

www.acsami.org Research Article

Continuous Synthesis and Processing of Covalent Organic Frameworks in a Flow Reactor

Safiya Khalil,* Abdullah Alazmi, Guanhui Gao, Cecilia Martínez-Jiménez, Ravindra Saxena, Yu Chen, Shu-Yan Jiang, Jianhua Li, Salma Alhashim, Thomas P. Senftle, Angel A. Martí, and Rafael Verduzco



Cite This: ACS Appl. Mater. Interfaces 2024, 16, 55206-55217



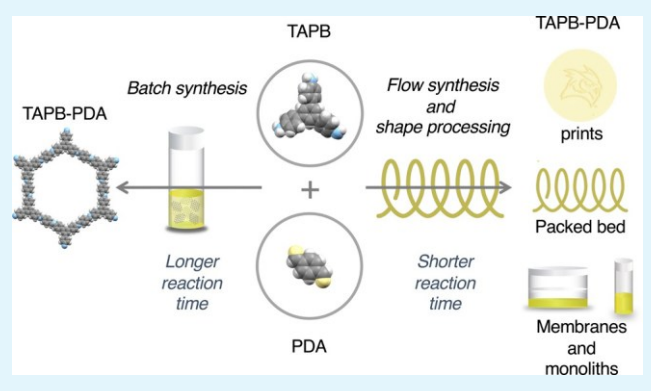
ACCES\$

III Metrics & More

Article Recommendations

Supporting Information

ABSTRACT: Covalent organic frameworks (COFs) are typically prepared in the form of insoluble microcrystalline powders using batch solvothermal reactions that are energy-intensive and require long annealing periods (>120 °C, >72 h). Thus, their wide-scale adoption in a variety of potential applications is impeded by complications related to synthesis, upscaling, and processing, which also compromise their commercialization. Here we report a strategy to address both the need for scalable synthesis and processing approaches through the continuous, accelerated synthesis, and processing of imine- and hydrazone-linked COFs using a flow microreactor. The flow microreactor is capable of unprecedented COF productivities, up to 61,111 kg m⁻³ day⁻¹, and provides control over key stages of COF formation, including nanoparticle



growth, self-assembly, and precipitation. Additionally, the technique successfully yields highly crystalline and porous COFs in versatile macroscopic structures such as monoliths, membranes, prints, and packed beds. We also show that a COF synthesized using the flow microreactor acts as an excellent photocatalyst for the photocatalytic degradation of perfluorooctanoic acid (PFOA) outperforming the degradation efficiency of its batch analogue and other classical photocatalysts such as titanium dioxide (TiO₂).

KEYWORDS: covalent organic frameworks, flow synthesis, processing, membranes, monoliths, prints, photocatalysis, photodegradation, perfluorooctanoic acid

INTRODUCTION

Covalent organic frameworks (COFs) are crystalline porous materials made by stitching organic molecules through robust covalent bonds. Unlike amorphous polymeric counterparts, COFs possess 2D or 3D long-range architectures determined by their monomeric topological diagrams.² Owing to their modularity and tunability, COFs have emerged as attractive candidates for various applications, including gas storage,3 photocatalysis, 4,5 separation, 6 and sensing. 7 While significant progress has been made in the development of new COF chemistries, linkages, and functionalities, several challenges still hinder their wide-scale commercialization and industrialization.8-11 This includes challenges associated with their synthesis, 12 upscaling, 13 and processing 14 to device-compatible formats.¹⁴ COFs are typically synthesized as microcrystalline powders in a batch process known as the solvothermal route,² which requires sealed pressurized tubes, elevated temperatures (120-200 °C), and long annealing periods (2-7 days).15 Additionally, this general batch synthesis route produces limited quantities of material per reaction requiring multiple batch processes for scaleup.^{8,13} Moreover, the resulting unprocessable powder makes it difficult to obtain device-compatible formats for application testing. These challenges translate to higher costs

and more difficult quality control of the final COF product. Thus, there is a growing demand for alternative, scalable synthesis approaches to processable COFs.¹³

Flow chemistry, which involves the use of microreactors or other flow reactors, is an attractive route for the preparation of porous crystalline materials. These flow systems offer a high surface-area-to-volume ratio, providing numerous advantages over traditional batch synthesis. ¹⁶ These advantages include precise control of reaction conditions, high mixing efficiency, ease of scale-up, improved heat and mass transfer, and safer handling of hazardous materials. ¹⁶ Table S1 shows a comparative summary on the advantages, limitations, and challenges of batch and flow techniques toward COF synthesis. Kobayashi and coworkers categorized continuous flow systems into several types (Type I–Type IV) based on the handling of reagents and catalysts. ¹⁷ In Type I systems, reagents pass

Received: June 10, 2024
Revised: August 28, 2024
Accepted: September 10, 2024
Published: September 18, 2024





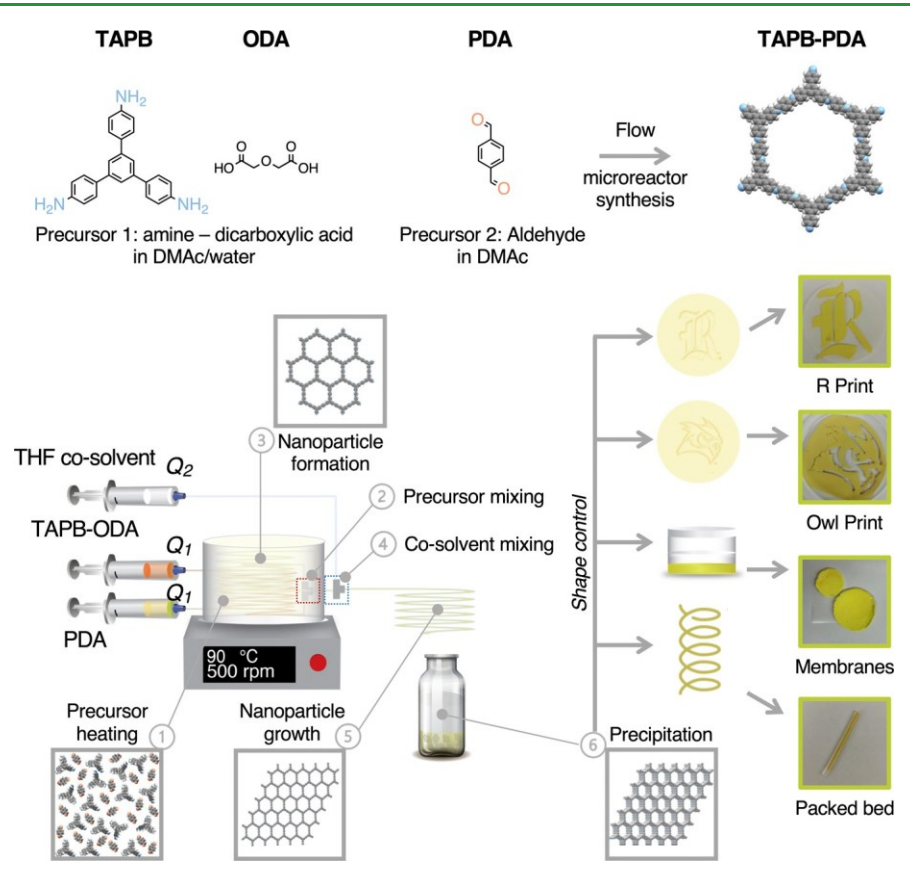


Figure 1. Overview of flow microreactor for the continuous high throughput synthesis and processing of a prototypical imine-linked COF. Top: amine and aldehyde precursor solutions used for flow synthesis of FrCOF-1. Bottom: schematic of microreactor modules and reaction setup. The red and blue dashed boxes indicate the microY mixers at 90 °C and room temperature, respectively. The numbers 1–6 illustrate the evolution of precursors injected into the microreactor to final COF bulk samples sequentially across the reactor modules. Right: controlled precipitation of FrCOF-1 to various macroscopic formats.

through a column or hollow loop where reactions occur without the separation of unreacted materials or byproducts in the absence of a catalyst. Type II systems operate without a catalyst and involve supporting one reagent in a column, which requires replacement once the substrate is depleted. Type III systems utilize a homogeneous catalyst, facilitating smooth reactions between reagents. Type IV systems employ a heterogeneous catalyst, eliminating the need for separation if catalysis proceeds efficiently. While numerous reports have demonstrated the successful flow synthesis of crystalline and porous materials like zeolites^{16,18} and metal-organic frameworks (MOFs)^{16,19-21} using Type III flow systems, their application to COF production has not been extensively explored due to a combination of challenges associated with the nature of COF synthesis.¹³ First, transitioning to continuous flow synthesis of COFs is not merely a matter of switching reactors and replicating batch conditions, as has been reported in previous studies on the flow synthesis of MOFs. 18 This is because the formation mechanisms of these materials are complex and vary based on the COF linkage. Second, COFs are linked by strong covalent bonds, and their reactions tend to be less reversible than those involving other porous materials such as MOFs.²² Consequently, they often require long annealing periods and high temperatures, while flow chemistry is designed for rapid reactions with faster kinetics. Lastly, COF particles tend to aggregate and precipitate uncontrollably during synthesis.¹³ This can potentially block the flow reactor tubing, disrupt precursor molar ratios, and prevent the formation of uniform

structures, making the flow synthesis route less feasible. Thus, translating COF synthesis from batch to flow synthesis requires optimization of many conditions that could potentially accelerate reaction kinetics in flow while avoiding particle aggregation. This involves screening temperatures, residence times, precursor flow rates, and concentrations under homogeneous reaction conditions.

The number of reports on the continuous flow synthesis of COFs, which encompasses both droplet-based approaches and continuous flow methods based on coflowing streams, remains limited. Unlike droplet-based synthesis methods, continuous flow synthesis under laminar conditions enables the mixing of precursor solutions solely via molecular diffusion, which promotes control over self-assembly events due to the controlled reaction-diffusion processes.¹³ One of the earliest examples of flow synthesis of COFs was reported by Puigmarti-Luis and coworkers, where they synthesized TAPB-BTCA imine-linked COF utilizing a four-inlet polydimethylsiloxane (PDMS) reactor operating at a very low Reynolds number.²³ Another approach, highlighted by Zhao and his team, demonstrated the continuous room-temperature synthesis of COF-LZU1 in polytetrafluoroethylene (PTFE) tubing.²⁴ They achieved a substantial production rate of 41 mg h⁻¹, with a space-time yield (STY) of 703 kg m⁻³ day⁻¹. Despite their success, both methods were only successful for a single COF chemistry, indicating the processes' specificity and the need for the monomers to be soluble in the solvent system. Additionally, it remained challenging to obtain films and bulk samples continuously in

flow. Dichtel and coworkers demonstrated the utility of a continuous flow approach to grow boronate ester-linked COF films on surfaces inside quartz crystal microbalance. However, this approach does not offer shape control of the sample, limiting processing to film configurations only. Although some progress has been made in obtaining film samples of boronate esterlinked COFs using flow systems, a corresponding advancement has not been accomplished for imine-linked COFs, which offer enhanced hydrolytic stability compared to their boronate esterlinked counterparts. This underscores a vital area for future research focused on developing methods to synthesize and process imine-linked COFs into bulk samples using flow synthesis systems.

Herein, we present a strategy for the continuous, accelerated synthesis and processing of imine- and hydrazone-linked COFs in a multistreamflow microreactor. The flow reactor modules are engineered to maintain control over key stages of COF formation including nanoparticle formation, growth, selfassembly, and precipitation. We demonstrate that this approach facilitates the processing of COFs to highly crystalline macroscopic structures such as monoliths, membranes, packed beds, and prints. Our flow synthesis microreactor enables the continuous production of a series of highly crystalline and porous imine- and hydrazone-linked COFs, with record productivities up to 61,111 kg m⁻³ day⁻¹. To determine the practical applicability of our methodology, we evaluated the performance of the FrCOF-4 "TAPT-DHTA" photocatalyst and its batch-synthesized analogue in the adsorption and photocatalytic degradation of PFOA. We found that FrCOF-4 is capable of adsorbing and degrading PFOA at room temperature and under mild conditions, outperforming the degradation efficiency of its batch-synthesized analogue and classical photocatalysts such as TiO₂. This work demonstrates the scalable production and processing of crystalline COF products, which can further promote their commercialization and industrialization.

EXPERIMENTAL SECTION

Microreactor Flow Synthesis of FrCOF-1-FrCOF-5. All FrCOF-1 to FrCOF-5 (Fr: Flow reactor) samples were synthesized using our microreactor flow synthesis strategy. FrCOF-1 was prepared by the condensation of 1,3,5-tris(4-aminophenyl)benzene (TAPB) with terephthalaldehyde (PDA) to form TAPB-PDA COF. FrCOF-2 was synthesized by the condensation of TAPB with 2,5-diethenyl-1,4benzenedicarboxaldehyde (PDA-V) to yield TAPB-PDA-V COF. FrCOF-3 was produced by the condensation of TAPB with 2,5dimethoxybenzene-1,4-dicarboxaldehyde (PDA-OMe) to create TAPB-PDA-OMe COF. FrCOF-4 was obtained through the condensation of 4,4',4"-(1,3,5-Triazine-2,4,6-triyl)trianiline (TAPT) with 2,5-dihydroxyterephthalaldehyde (DHTA) to form TAPT-DHTA COF. Finally, FrCOF-5 was prepared by the condensation of 2,5diethoxyterephthalohydrazide (DETH) with 1,3,5-tris(4formylphenyl)benzene (TFB) to form DETH-TFB COF. All samples were synthesized as bulk monolithic samples with yields ranging from 93 to 95%. After purification and drying, the structural properties of each sample were studied. For the FrCOF-4 photocatalyst, the structural, morphological, photoelectrochemical, and optoelectronic properties were assessed, before it was applied for PFOA adsorption and photocatalytic degradation.

RESULTS AND DISCUSSION

Continuous Flow Synthesis of a Prototypical COF. Our microreactor flow synthesis strategy is systematically illustrated in Figure 1 using TAPB and PDA as building blocks for the synthesis of TAPB-PDA, referred to as FrCOF-1 (Fr: Flow

reactor), which serves as a prototypical imine-linked COF. The microreactor consists of three distinct modules: injection, reaction, and shape processing (see Figure S1 for details on modules and their respective components). These modules are assembled to control the key stages of COF formation including COF nanoparticle formation, growth, self-assembly, and precipitation (Figure 1). First, the injection module introduces precursor solutions and solvents at precisely controlled volumetric flow rates. The solutions then proceed to the reactor module, which enables the formation and growth of COF nanoparticles while preventing precipitation and aggregation. Finally, the process transitions to the shape processing module, which facilitates the self-assembly and processing of COF nanoparticles into desired physical formats, including membranes, prints, and packed beds.

The injection module utilizes a syringe pump to introduce precursor solutions into 1/16-in. inner diameter PTFE tubing at the desired stoichiometry. In the configuration shown in Figure 1, precursor 1 ("TAPB-ODA") is a solution of TAPB and diglycolic acid (ODA) dissolved in dimethylacetamide (DMAc) and water, while precursor 2 ("PDA") is a solution of PDA in DMAc. Each precursor is injected into a separate PTFE tube. These tubes are immersed in an oil bath at 90 °C, rapidly heating the precursor solutions to 90 °C. Subsequently, the preheated precursors proceed to the reactor module where they are mixed by a polyetheretherketone (PEEK) microY mixer also immersed in the oil bath at 90 °C (see the red dashed box in Figure 1). The mixer ensures thorough mixing of the precursor streams and initiates the reaction, producing an outlet stream at 90 °C. The COF formation process occurs in a microtubular reactor maintained at a consistent temperature of 90 °C. Upon exiting the oil bath, the COF nanoparticle stream is quenched by injecting tetrahydrofuran (THF) cosolvent and mixing both streams in another microY-mixer at room temperature (see the blue dashed box in Figure 1). The nanoparticle suspension then proceeds through a predefined length of tubing at room temperature, promoting their growth without precipitation or gelation. The COF nanoparticles stream subsequently enters the shape processing module, where the nanoparticles are continuously precipitated in a hexane bath. This controlled precipitation step allows for the processing of COF nanoparticles into bulk samples of desirable shape and size continuously within the flow reactor scheme. The detailed procedures for obtaining these various macroscopic formats can be found in Note S1 and Table S2. The bulk samples were first soaked in hexane overnight, then washed using THF and ethanol, followed by supercritical carbon dioxide (ScCO₂) drying to yield FrCOF-1 monoliths, membranes, and prints (Figure 1). Details on the flow reactor components and PTFE tubing lengths in the different reactor modules are provided in the Figure S1 and Table S3. The key differences between our microreactor strategy and previously reported flow synthesis methods for COFs and MOFs are summarized in Note S2 and Table S4.

To promote the self-assembly of COF nanoparticles and enhance product crystallinity, we incorporated ODA as a catalyst in the flow microreactor. In a previous study, we compared the batch synthesis process with and without ODA to illustrate its impact on the synthesis process and the properties of the resulting COFs.²⁶ We found that samples made using acetic acid (AcOH) as a catalyst exhibited poor crystallinity compared to those synthesized with ODA. Further investigation showed that the COF amine monomer and ODA underwent a

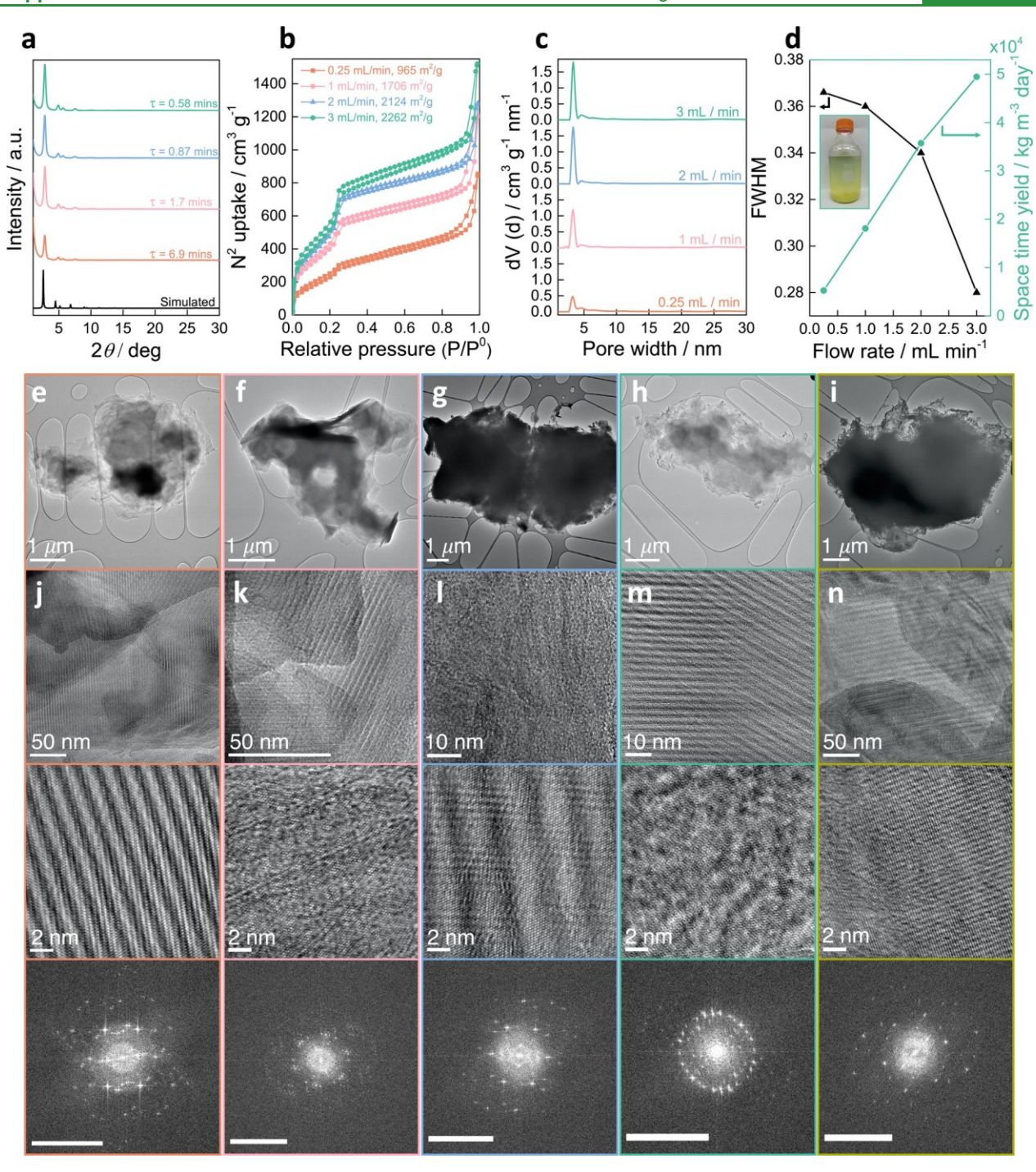


Figure 2. Effect of residence time and concentration on the prototypical FrCOF-1 ("TAPB-PDA") synthesized by microreactor. (a) PXRD patterns show full crystallinity regardless of operating flow rate. (b) N_2 adsorption isotherms showing increasing porosity at shorter residence times. (c) Total pore volumes increase with reducing residence time. (d) fwhm (black) decreases and STY (mint) increases for higher flow rates. TEM and HRTEM images with fast Fourier Transforms (FFT) for FrCOF-1 synthesized at inlet precursor flow rates of (e,j) 0.25 mL min⁻¹, (f,k) 1 mL min⁻¹, (g,l) 2 mL min⁻¹, (h,m) 3 mL min⁻¹, and (i,n) 3 mL min⁻¹ (1/2 concentration), respectively. The scale bar of all FFTs is 10 nm⁻¹.

self-assembly process in DMAc solvent. The amine-ODA system in DMAc exhibited a thermoreversible solution-to-gel transition, indicating the formation of supramolecular organic gels at room temperature. In contrast, the TAPB- AcOH system in DMAc did not gel at room temperature. This self-assembly process involving amine-ODA in DMAc enhances the final crystallinity of imine COFs synthesized with ODA. We also compared the rate of growth of COF nanoparticles as they cooled to room temperature using dynamic light scattering (DLS) technique.

Our findings demonstrated that ODA significantly enhanced the growth rate of COF nanoparticles compared to AcOH.

To prevent precipitation in the flow microreactor, we implemented a solvent polarity engineering strategy across the flow reactor modules. In a previous study, we reported homogeneous conditions that achieved a stable suspension of COF nanoparticles, free of aggregation or precipitation, at temperatures of 80 °C or higher.²⁶ This produced a COF gel upon cooling to room temperature. As previously demonstrated

using dynamic light scattering (DLS) measurements, under these conditions, COF crystallites grow and remain in solution at elevated temperatures. A similar approach, combined with the solvent polarity engineering strategy, was implemented in the continuous flow microreactor to avoid gelation of nanoparticles as they cool to room temperature, thereby facilitating their shape processing into desired macroscopic formats. First, separate solutions of ODA and TAPB were blended with PDA at 90 °C to initiate COF synthesis. In the hot reaction zone, the mixture initially had a polarity index of approximately 6.527 (see Table S5 for polarity indices of solvent systems). Next, THF was injected as a stabilizing cosolvent, cooling down the hot stream of COF nanoparticles suspension to room temperature while preventing precipitation. This was executed in a 1/1 v/v ratio into the COF nanoparticles stream, resulting in a drop of the mixture polarity index to around 5.25 in the cold reaction zone. This reduction affects the rate of COF nanoparticle formation and suppresses the gelation process at room temperature. DLS analysis further supports this, showing that using THF as a cosolvent stabilizes the resultant mixture during the growth process, avoiding nanoparticle aggregation or gelation even at room temperature (Figures S2 and S3).

We characterized the crystallinity, porosity, and morphology of FrCOF-1 synthesized using the flow reactor with varying residence times, which were controlled by adjusting the rate of precursor solution injection (0.25 mL min⁻¹ to 10 mL min⁻¹) with an automated syringe pump. The total residence time is defined as time taken from the precursor mixer stage to the precipitation stage which varied from approximately 0.2 to 7 min. More details on total residence time estimation including hot and cold reaction zones are provided in Table S6. For these tests, we used our benchmark homogeneous batch reaction conditions as a reference point, with an initial precursor molar concentration of 0.667 mmol of TAPB and 1 mmol of ODA in DMAc/water mixture (5.6 mL/1.4 mL) and 1 mmol of PDA in DMAc (7 mL), and we produced solid COF monolith samples.

The formation of FrCOF-1 at various residence times was confirmed using Fourier transform infrared (FTIR) spectroscopy and powder X-ray diffraction (PXRD). FTIR analysis of FrCOF-1 confirmed the successful formation of the imine bond (C□N) with a stretching band observed at ~1617 cm⁻¹ (Figure S4). While all FrCOF-1 IR spectra displayed a complete absence of amino groups, weak carbonyl (C□O) group vibrations (~1685 cm⁻¹) were present. This suggests a complete reaction occurred between monomeric units in the microreactor, with some unreacted groups remaining within the COF nanoshets.

The PXRD patterns of FrCOF-1 prepared at various residence times showed excellent crystallinity and matched the simulated pattern of TAPB-PDA imine COF (Figure 2a). The monolithic COF samples showed diffraction peaks at 2.8°,4.9°, 5.6°, and 7.5° attributed to the (100), (110), (200), and (210) planes, respectively.

The permanent porosity of FrCOF-1 bulk monolithic samples was evaluated using nitrogen adsorption isotherms measured at 77 K and 1 atm (Figure 2b). Detailed procedures for sample preparation for nitrogen sorption measurements are available in Supplementary Methods 1.2.4. The calculated Brunauer—Emmett—Teller (BET) surface areas of FrCOF-1 monolithic samples increased as the residence time in the flow reactor decreased, reaching up to 2262 m² g⁻¹ at a residence time of 0.58 min (Figure 2b). This BET surface area at a residence time of 0.58 min approaches the theoretical Connolly surface area of TAPB-PDA COF, which is 2600 m² g⁻¹.28 Simultaneously, the

total pore volume also increased as the residence time in the flow reactor decreased, peaking at 1.8 cm³ g⁻¹ (Figure 2c). Additionally, we observed that the full-width-at-half-maximum (fwhm) of the (100) peak in the PXRD patterns of FrCOF-1 decreased as the residence time shortened (Figure 2d). At shorter residence times, there is less time for crystal growth, leading to the formation of smaller COF nanosheets. These smaller nanosheets likely stack more easily, forming more ordered crystallites and resulting in a sharper 100 Bragg reflection, corresponding to a lower fwhm. The formation of well-stacked 2D COF material with more accessible voids at shorter residence times likely accounts for the observed increase in BET surface area as the residence time decreases.

The overall efficiency of the microreactor in producing FrCOF-1 was quantified by estimating the space-time yield (STY), which is defined as the mass of COF product (kg) per unit reactor volume (m³) per unit time (days of synthesis) (see Note S7 for STY estimation). We examined various factors that influence the STY of FrCOF-1, such as the inlet precursor flow rate and precursor concentration (Table S7). Our analysis of Table S7 reveals that increasing the inlet precursor flow rate enhances STY, whereas lowering the precursor concentration reduces STY. Among the conditions tested, operating the flow reactor at a reduced residence time of 0.58 min (inlet precursor flow rate of 3 mL min⁻¹) yielded crystalline FrCOF-1 at a high STY of 49,471 kg m⁻³ day⁻¹ (Figure 2d). Achieving such a high STY in the microreactor is crucial for maximizing COF production rates while minimizing reactor volume, thereby promoting industrial scalability and cost-effectiveness.

We also investigated the effect of operating the reactor at a very low residence time of 0.17 min (inlet precursor flow rate 10 mL min⁻¹) on the formation of FrCOF-1. PXRD analysis of the sample formed under these conditions confirmed the successful formation of crystalline FrCOF-1, even at such a low residence time (Figure S6). This analysis showed that the material retained its crystalline structure at a significantly improved STY of 125,324 kg m⁻³ day⁻¹ (Table S7). Thermogravimetric analysis (TGA) provided evidence of the thermal stability of FrCOF-1 synthesized at very short residence times (Figure \$5). However, the sample exhibited a lower BET surface area (1000 m² g⁻¹) as confirmed by N₂ sorption analysis (Figure S7). Additionally, analysis of pore size distribution revealed a smaller pore volume (\sim 0.6 cm³ g⁻¹, Figure S8). These findings suggest that the observed increase in STY at a residence time of 0.17 min or lower results in a reduced surface area of the synthesized sample. Therefore, there is a trade-off between the production rate and the COF crystallinity at very short residence times.

We further investigated the effect of residence time while maintaining consistent fluid dynamics on the formation of FrCOF-1. This was accomplished by keeping the flow rate constant (inlet precursor flow rate of 1 mL min⁻¹) and varying the tubing length. The total residence time, defined as the duration from the precursor mixing stage to the precipitation stage, was adjusted from approximately 1.7 to 8.5 min. Additional details regarding the estimation of total residence time, including the hot and cold reaction zones as well as the tubing lengths of the reactor, are provided in Tables S8 and S9, respectively. FTIR analysis confirmed the successful formation of the imine bond $(C \square N)$ with a characteristic stretching band at approximately 1617 cm⁻¹ observed consistently across both conditions (Figure S9). Further characterization through TGA analysis verified the thermal stability of FrCOF-1 at both shorter and extended residence times (Figure S10). Notably, PXRD

analysis revealed that operating at a higher residence time (τ = 8.5 min) yields more crystalline FrCOF-1 (Figure S11), as evidenced by a lower fwhm of the (100) peak (fwhm = 0.26). Moreover, the sample demonstrated a higher BET surface area of 1808 m² g⁻¹ as confirmed by N₂ sorption analysis (Figure S12), and pore size distribution analysis highlighted a substantial pore volume (\sim 3 cm³ g⁻¹, Figure S13). However, the STY at a higher residence time (τ = 8.5 min) dropped to 1,790 kg m⁻³ day⁻¹, compared to 18,096 kg m⁻³ day⁻¹ at a shorter residence time (τ = 1.7 min, see Table S7). These findings illustrate that extending the residence time in the reactor, while keeping fluid dynamics stable, allows more time for crystal growth, thereby enhancing the crystallinity and porosity of the COF. However, this benefit comes with a trade-off in the production rate at longer residence times.

We further examined the effect of precursor concentration on the formation of FrCOF-1. PXRD analysis confirmed that even at a lower precursor concentration (0.33 mmol of TAPB and 0.5 mmol of ODA in DMAc/water mixture (5.6 mL/1.4 mL) and 0.5 mmol of PDA in DMAc (7 mL)), a highly crystalline FrCOF-1 could be formed (Figure S14). However, N₂ sorption analysis (Figure S15) revealed a decreased BET surface area (1445 m² g⁻¹) and smaller pore volume (approximately 0.8 cm³ g⁻¹, Figure S16). Additionally, operating at a lower concentration resulted in a large drop in STY to 12,609 kg m⁻³ day⁻¹ compared to 49,471 kg m⁻³ day⁻¹ at a higher precursor molar concentration for the same inlet precursor operational flow rate (3 mL min⁻¹, Figure S17 and Table S7).

We studied the effect of alternative stabilizing cosolvents on the crystallinity of COFs using our microreactor flow synthesis strategy. Previous studies have reported the role of nitrile cosolvents as stabilizing agents in the synthesis of boronate ester- and imine-linked COFs.^{29,30} Therefore, we explored the impact of acetonitrile (MeCN) as an alternative cosolvent to THF (at a precursor inlet flow rate of 3 mL min⁻¹). See Note S8 for experimental details. The microreactor performed efficiently without any clogging issues over a residence time of 1.7 min, and a FrCOF-1 monolith was obtained. FTIR analysis of the washed and dried FrCOF-1 synthesized using MeCN cosolvent confirmed the formation of the imine bond ($C\square N$), characterized by a stretching band at approximately 1617 cm⁻¹ (Figure S18). The PXRD pattern of FrCOF-1 exhibited good crystallinity, closely matching the simulated pattern of the TAPB-PDA imine COF with diffraction peaks at 2.8°, 4.9°, 5.6°, and 7.5°, corresponding to the (100), (110), (200), and (210) planes, respectively (Figure S19). While both FTIR and PXRD analyses confirmed the successful synthesis of crystalline iminelinked FrCOF-1, our results indicated a significantly reduced gelation period of approximately 3 min upon incorporating MeCN cosolvent (1/1 v/v). In contrast, THF cosolvent completely stabilized the suspension without any gelation. We attribute this behavior of MeCN cosolvent to its higher polarity index compared to THF (Table S5). Specifically, substituting THF with MeCN increased the solvent system polarity index from 5.25 to 6.15 (see Table S5 for polarity index estimations). This finding suggests that nitrile cosolvents such as MeCN can disrupt gelation in the microreactor for a limited period, reducing the operable residence time range. Therefore, the use of MeCN as a cosolvent may not be the most suitable stabilizing agent for studying other chemistries with stronger π – π interactions or hydrogen bonding which often have a higher gelation speed compared to TAPB-PDA COF chemistry.

We investigated the quality of FrCOF-1 produced after operating the reactor at a residence time of 0.58 min (inlet precursor flow rate 3 mL min⁻¹) for approximately ~10 min (inset image in Figure 2d) to evaluate the overall scalability of the microreactor (Movie S1). A total sample mass of approximately 1.2 g was produced. PXRD analysis confirmed that the scaled-up FrCOF-1 sample had excellent crystallinity (Figure S20). The calculated BET surface area (2249 m² g⁻¹) from N₂ sorption analysis (Figure S21) further confirmed the excellent permanent porosity of the scaled-up FrCOF-1 sample. Additionally, the scaled-up sample possessed a high total pore volume of 2.25 cm 3 g $^{-1}$ (Figure S22). TGA analysis of the scaled-up synthesis of FrCOF-1 exactly matched that of FrCOF-1 produced at an inlet precursor flow rate of 3 mL min⁻¹ (Figure S5), confirming its thermal stability. This shows that the flow microreactor can be implemented for high throughput production of crystalline and porous COFs.

We used transmission electron microscopy (TEM) to elucidate the effect of residence time and concentration on the microstructure of FrCOF-1. All samples exhibited clear crystalline lattice indicating that the materials were highly crystalline (Figures 2e-n and S23a-d). There was a clear trend in which the decline in residence time corresponded to a reduction in the dimension of the COF sheets (Figures 2e-h and S23a). In the same context, the precursor mixture concentration appeared to play a pivotal role in the determination of FrCOF-1 sheet size. Maintaining a consistent residence time under a precursor flow rate of 3 mL min⁻¹, a diluted precursor concentration corresponded to significantly larger COF sheets (Figure 2h,i). This observation suggests that a reduced precursor concentration results in a lower nucleation rate which means less competition for available precursors resulting in the formation of larger sheets. This suggests that precursor concentration stimulates nucleation, however, it does not similarly augment growth.

Scope of the Microreactor COF Synthesis Method. Next, we demonstrated the generality and versatility of our continuous flow reactor approach through the preparation of four more imine- and hydrazone-linked COF chemistries that were previously synthesized using solvothermal synthesis: FrCOF-2 ("TAPB-PDA-V"), FrCOF-3 ("TAPB-PDA-OMe"), FrCOF-4 ("TAPT-DHTA"), and FrCOF-5 ("DETH-TFB"). The synthesis of FrCOF-2-FrCOF-5 was performed under optimized conditions of residence time and precursor molar concentration (refer to Note S3 for more details on synthesis), enabling the rapid production of functional COFs. All these imine and hydrazone COFs exhibit a hexagonal topology. Notably, TAPB-PDA-V provides an excellent platform for postsynthetic modification and tuning of pore functionality,³¹ rendering it a highly versatile framework applicable to a wide range of applications, including separation and adsorption. Similarly, TAPB- PDA-OMe, with its methoxy side groups, forms a robust framework suitable for postsynthetic modification. The resonance effect generated by these groups promotes framework crystallization and π – π stacking.³² TAPT-DHTA, composed of photoactive counterparts with donor-acceptor characteristics, is known for its photocatalytic potential.33

Our study demonstrates that the microreactor flow synthesis strategy can be effectively applied for the synthesis of COFs with various linkages, including hydrazone (refer to Note S3 for a detailed synthesis, Figure S24 and Table S10). We assessed the quality of COFs produced using the microreactor using FTIR spectroscopy, TGA, PXRD, and N₂ sorption analysis. The

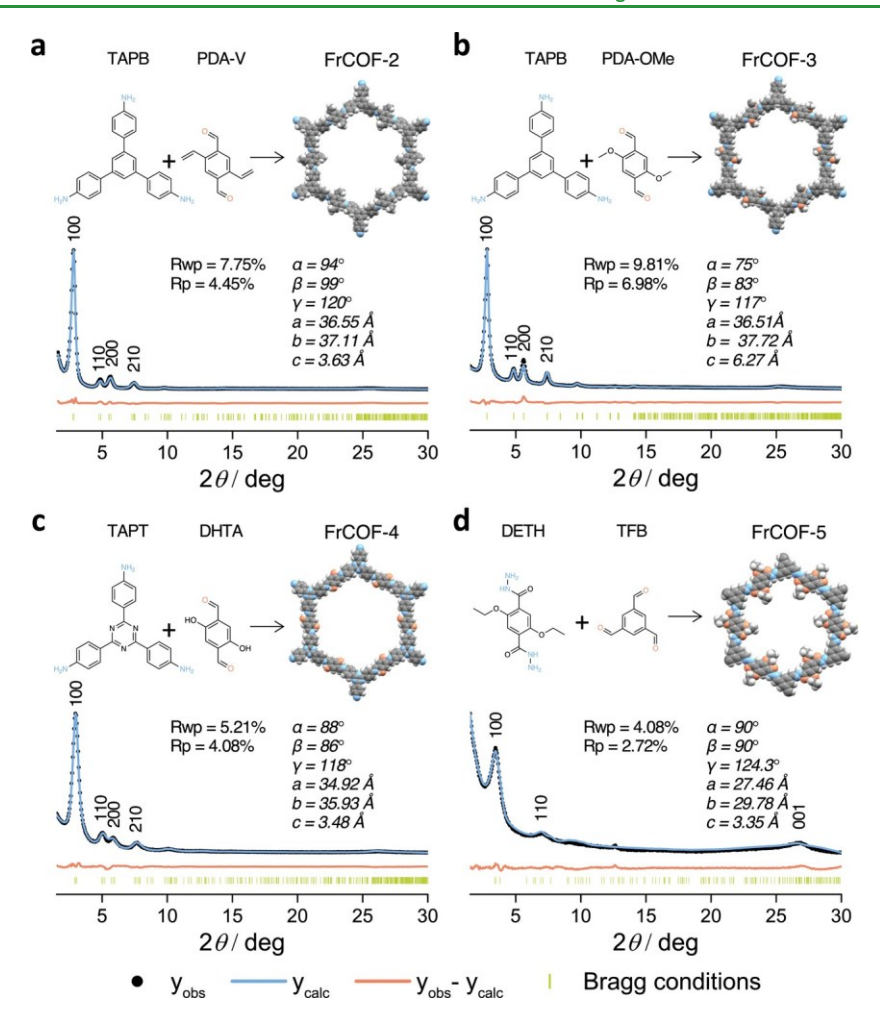


Figure 3. High throughput continuous synthesis of imine and hydrazone COFs in microreactor. (a--d) Synthetic scheme for FrCOF-2-FrCOF-5 along with Pawley refinements of FrCOF-2-FrCOF-5 with their respective PXRD patterns.

successful formation of the imine bond (C□N) in all FrCOFs was evident through vibrations detected at approximately 1614–1618 cm⁻¹ (see Figures S25–S28). Weak carbonyl $(\sim 1662-1689 \text{ cm}^{-1})$ groups were present in the IR spectra due to unreacted end groups across the COF nanosheets. An additional vibration related to the amide group (C□O) was evident in FrCOF-5 at approximately 1659 cm⁻¹. The thermal stability of FrCOF-2 - FrCOF-5 samples was confirmed using TGA under a nitrogen atmosphere (Figure S29). While PXRD patterns confirmed the excellent crystallinity of the imine-linked FrCOF-2 – FrCOF-4 samples (Figure 3a – c), the hydrazonelinked FrCOF-5 sample did not exhibit the same level of crystallinity (Figure 3d). This discrepancy could be due to the application of optimized conditions for imine linkage (inlet precursor flow rate, residence time, precursor concentrations) to the hydrazone COF chemistry to validate the universality of the microreactor flow synthesis strategy. Despite each chemistry having its kinetics of formation, these results indicate that while the microreactor flow synthesis strategy is broadly applicable, certain COF linkages like hydrazone (FrCOF-5) may require further optimization of residence time, flow rate, and precursor concentration. Such optimization is necessary to align the kinetics of formation with the reactor's residence time and achieve higher crystallinity. Moreover, Pawley refinements showed an excellent fit between simulated and experimental PXRD patterns of FrCOF-2-FrCOF-5 (Tables S11-S14). The

permanent porosity of the FrCOFs was examined via nitrogen sorption analysis, conducted at a temperature of 77 K. All iminelinked COF samples had excellent BET surface areas (Figure S30) and pore size distributions (Figure S31). In contrast, while the hydrazone-linked FrCOF-5 sample had a good BET surface area (Figure S30), its pore size distribution was wide (Figure S31). The BET surface areas of all FrCOF-2 through FrCOF-5 samples were compared with those reported for solvothermal analogs in the literature (Table S15). All COF samples generally displayed comparable, if not enhanced, BET surface areas (Table S15). The STY for these frameworks gives a clear indication of the reactor's efficiency: FrCOF-2 yielded 61,111 kg m⁻³ day⁻¹, FrCOF-3 produced around 34,920 kg m⁻³ day⁻¹, FrCOF-4 generated close to 45,746 kg m⁻³ day⁻¹, and FrCOF-5 formed 49,670 kg m⁻³ day⁻¹ (Table S7). Thus, this process allows for the scaled-up synthesis of imine and hydrazone COF frameworks and could be optimized for other linkages. All the synthesized samples were produced as bulk samples in the form of membranes or monoliths (Figure S32).

Microstructure and Optical Properties of Photoactive FrCOF-4. COFs have recently emerged as a promising material platform in heterogeneous catalysis for photocatalytic aqueous pollutant treatment. 4,34,35 Donor—Acceptor (D-A) COFs, which can be synthesized from an extensive array of monomers, may exhibit varying degrees of photocatalytic activity. COFs with extended π -conjugated structures can absorb broadly out to

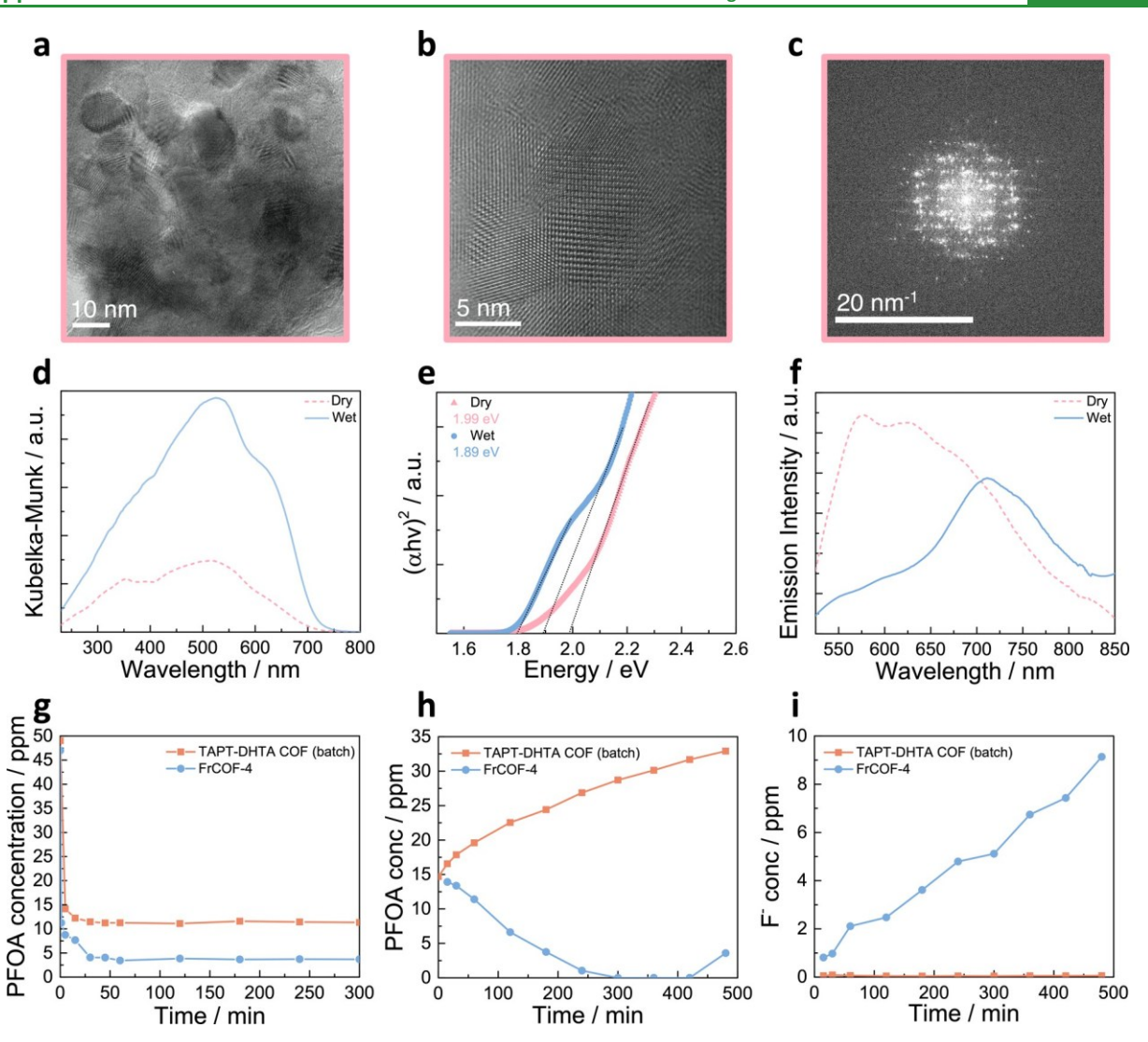


Figure 4. Characterization and photocatalytic degradation of PFOA by FrCOF-4. (a) TEM and (b) HRTEM image of FrCOF-4 and its corresponding (c) FFT. (d) DR-UV—vis spectra of dry and wet FrCOF-4. (e) Normalized Tauc plots from UV—vis spectra for direct band gap. Dashed lines best linear fits to the absorption edges. (f) PL emission spectra of dry and wet FrCOF-4. The excitation wavelength was ~540 nm. (g) HPLC detected concentration—time profiles of PFOA for batch-grown TAPT-DHTA and FrCOF-4 without irradiation. (h) HPLC-detected concentration—time profiles of PFOA for batch-grown TAPT-DHTA and FrCOF-4 with 254 nm irradiation. (i) IC-detected concentration—time profiles of fluoride ion (F—) with 254 nm irradiation. Reaction conditions: [PFOA]0 = 46.7 ppm, COF dosage of 1 g L⁻¹ in 50 mL PFOA solution, 254 nm UV—C light, initial pH of 3.2, ambient conditions.

visible-light wavelengths, and the $\pi-\pi$ layered stacking results in electronic overlapping, thereby providing sufficient pathways for charge carrier (electron, (e–) and hole, (h+)) separation.³⁶ FrCOF-4, synthesized as bulk samples via our flow reactor strategy, is composed of a D–A structure, which makes it a promising candidate for photocatalysis.³³ High crystallinity is thought to be useful for photocatalytic performance due to improved charge carrier transport in the COF.³⁷ Besides PXRD analysis (Figure 3c), the crystallinity of FrCOF-4 was further analyzed using High-Resolution Transmission Electron Microscopy (HRTEM), which revealed excellent crystallinity and diffraction (Figure 4a–c).

The absorbance of FrCOF-4 was assessed and compared to its monomeric building blocks using diffuse reflectance ultraviolet—visible (DR-UV—vis) spectroscopy (Figure S31). FrCOF-4 exhibited a much broader and red-shifted band compared to its monomeric counterparts, due to increased conjugation length in the COF (Figure S33). The energy band

gap was calculated from Tauc plots (Figure 4e), revealing a bandgap of 1.99 eV. Additionally, the photoluminescence (PL) emission spectra of FrCOF-4 relative to its monomeric counterparts revealed lower photoluminescence in the COF (Figure S34).

Besides FrCOF-4 optical properties in dry conditions, the material possesses distinct optical properties in its hydrated form (Figure S35). Notably, FrCOF-4 undergoes color transition from red to black when exposed to water, and this color change is readily reversible (Figure S35). We attribute this distinct change in color to the rapid and dynamic iminol to ketoenamine equilibrium, mirroring a phenomenon previously observed and reported earlier for TAPB-PDA-OH COF by Marder and coworkers.³⁸ We employed density functional theory (DFT) to confirm the feasibility of the proposed tautomerization reaction. The computed reconstruction free energy (-0.33 eV) provides solid evidence supporting the structural transformation of FrCOF-4 upon exposure to water (Figure S36a-c). We

analyzed the effect of this transition on the optical properties of FrCOF-4 using DR-UV-vis spectroscopy and PL emission. The DR-UV spectrum of the wet form of FrCOF-4 showed the emergence of a shoulder at longer wavelengths (~620 nm, Figure 4d). This is consistent with previous reports that provide density functional theory (DFT) and experimental evidence that iminol/cisketoenamine absorbs at longer wavelength than the diiminol and indicate that this absorption has significant chargetransfer character.³⁸ The energy band gap for the hydrated FrCOF-4, as extrapolated from the Tauc plots (Figure 4e), indicated a decline from 1.99 eV (dry) to 1.89 eV (wet). In addition, a comparison of the PL spectra between the hydrated and dry states of FrCOF-4 revealed a shift in the PL wavelength to 720 nm, accompanied by a diminished PL emission intensity in the hydrated state (Figure 4f). This suggests that FrCOF-4 is an excellent photocatalyst in aqueous environments, primarily attributable to its distinctive properties when hydrated as opposed to its dry state. We further explored the electronic property change following the tautomerization reaction of FrCOF-4 and observed a decrease in the band gap due to the structural change, which is consistent with the experimental findings and further implies the excellent photocatalytic properties of the hydrated form of FrCOF-4 (Figure S34a-c). We examined the photoelectrochemical characteristics of FrCOF-4 by performing cyclic voltammetry and linear sweep voltammetry (LSV) in the potential range -0.6 to 0.6 V (refer to Methods S1.2.9 and S1.2.10 for details on sample preparation and device testing, Figures S37 and S38). To further assess the photoactivity of FrCOF-4, we used it as a photocathode at 0.2 V under blue light, in a 0.1 Na₂SO₄ liquid electrolyte, and tracked photogenerated currents (refer to Methods S1.2.9 and S1.2.11 for details on sample preparation, concentration, and photocurrent test). The deposited FrCOF-4 sample exhibited a photocurrent density of approximately 0.02 μ A cm⁻² which demonstrates that FrCOF-4 is photoactive (Figure S39)

Adsorption and Photocatalytic Degradation of PFOA. We investigated the use of FrCOF-4 for the adsorption and photocatalytic degradation of PFOA to produce innocuous chemicals. The pH of the solution affects the existing form of PFOA (deprotonated/protonated) as well as the COF. Therefore, to find the optimal pH that promotes PFOA-FrCOF-4 interactions, we assessed the isoelectric point (where zeta potential = 0) of FrCOF-4 using zeta potential measurements (Figure S41) by suspending FrCOF-4 in buffer solutions ranging from pH = 1-6 (Figure S40). FrCOF-4 samples suspended in the various pH buffers appear in different colors. At a pH > 3, the samples appear as brown agglomerates (Figure S40). On the other hand, at pH 3 and lower, the samples appear to be suspended as red fine particulates (Figure S40). As depicted from the zeta potential profile as a function of pH, FrCOF-4 has an isoelectric point at a pH of approximately 3 (Figure S41). This implies that the COF has a net positive charge at $pH < pH_{pzc}$. We then assessed the kinetics of adsorption at a pH of 2.5 and 3.2, respectively (Figures 4g and S42). Under both pH conditions, PFOA exists predominantly in its deprotonated form due to the pH being higher than its pK_a . 50 mg of dry COF was mixed with approximately 50 ppm PFOA at a concentration of 1 g L^{-1} in solutions with pH = 2.5 and pH = 3.2, respectively, in the dark. Then \sim 0.6 mL aliquot samples were taken and analyzed by high-performance liquid chromatography with diode-array detection (HPLC-DAD) to determine PFOA concentration at different time points. It took FrCOF-4 approximately 25 min to saturate at a pH of 3.2

(Figure 4g) and 15 min at a pH of 2.5 (Figure S42). Additionally, FrCOF-4 adsorbed 92% of PFOA in 25 min at a pH of 3.2 (Figure 4g) and 98% of PFOA in 15 min at a pH of 2.5 (Figure S42). These measurements indicate that operating at a lower pH could improve adsorption kinetics and capacity. However, for safety and to avoid the formation of HF, we performed degradation at a pH of 3.2.

To compare the adsorption and photocatalytic degradation of FrCOF-4 with its batch analogue, we synthesized TAPT-DHTA COF via batch synthesis using identical concentrations, solvent systems, and mixing protocols. Details of the synthesis route are provided in Note S4. FTIR analysis confirmed the successful formation of TAPT-DHTA batch-grown COF, with the imine bond (C□N) stretching band observed at ~1617 cm⁻¹ (Figure S43). Weak carbonyl ($C\square O$) group vibrations were present at ~1663 cm⁻¹ (Figure S43). While PXRD analysis indicated that the sample is crystalline, the crystallinity was found to be susceptible to compromise during sample grinding for PXRD sample preparation (Figure S44). This susceptibility is illustrated by the increase in the fwhm from 0.49 to 0.62 upon grinding. Therefore, N₂ sorption analysis was performed on the bulk sample without any grinding, revealing a high BET surface area of 3608 m² g⁻¹ (Figure S45) and a pore volume of 2.4 cm³ (Figure S46). TGA analysis confirmed the thermal stability of batch-synthesized TAPT-DHTA COF (Figure S47).

Before irradiation with 254 nm UV-C light, FrCOF-4, and its batch-synthesized analogue were stirred in a 50 ppm PFOA solution (pH = 3.2) in the dark for 5 h to achieve equilibration (Figure S48a). The adsorption kinetics were then fitted using a pseudo-second-order kinetics model, resulting in a high correlation coefficient ($R^2 = 0.99998$) (details in Note S5, Table S16 and Figure S48b,c), and yielding rate constants of k_2 = 2.66 g mg⁻¹ h⁻¹ for FrCOF-4 and k_2 = 16.7 g mg⁻¹ h⁻¹ for its batch-synthesized analogue. However, FrCOF-4 exhibited a higher adsorption capacity of $q_e = 43.4 \text{ mg g}^{-1}$ compared to its batch-synthesized counterpart with $q_e = 37.6 \text{ mg g}^{-1}$ (Table S16). This could be attributed to the higher crystallinity of FrCOF-4 relative to its batch-synthesized analogue which allows for more accessible and efficient adsorption sites, enhancing the overall adsorption capacity. Subsequently, the suspensions containing saturated FrCOF-4 and the batch analogue were exposed to 254 nm UV-C light for approximately 8 h to study the photodegradation kinetics of PFOA (see reactor schematic in Figure S49). Aliquot samples were periodically taken and analyzed by HPLC and Ion Chromatography (IC) to monitor the concentrations of PFOA and fluoride ions in the suspensions throughout the photocatalytic degradation reactions. After 8 h, we observed a drop in PFOA concentration in bulk solution to 3.6 ppm in the suspension containing FrCOF-4 photocatalyst (Figure 4h). Additionally, 9.4 ppm of fluoride ions were detected in the same suspension (Figure 4i), reflecting PFOA degradation and the cleavage of C-F bonds. This concentration corresponds to 28% degradation of the initial 46.7 ppm PFOA solution (see Supporting Methods 1.2.14 for % degradation estimation). Correspondingly, this is equivalent to a first-order rate constant of $k_t = 0.0064 \text{ min}^{-1}$ (see Note S6 for details on first-order rate constant estimation) for the degradation of PFOA, and compares favorably to that of other photocatalysts, such as TiO₂, tested under similar conditions (Table S17). A comparison of the k_t values clearly shows that FrCOF-4 (k_t = 0.0064) outperforms TiO₂ ($k_t = 0.0001$), achieving a much higher rate constant at substantially lower light energy (Table S17). This result is very promising, and we expect that with

further screening and optimization of catalyst dosage, light energy, and reaction period, FrCOF-4 degradation efficiency can be drastically improved. Conversely, in the suspension containing the batch-synthesized analogue to the FrCOF-4 photocatalyst, we detected a constant increase in PFOA concentration to 32.9 ppm (Figure 4h). Analysis of these aliquots by IC showed almost no fluoride ions (Figure 4i), suggesting either no significant degradation of PFOA occurred or adsorption of the fluoride ions onto the COF sample. Since sample crystallinity is the most important factor governing degradation, the rapid loss of crystallinity in the batchsynthesized TAPT-DHTA COF sample upon grinding for adsorption and degradation tests renders it less effective as a photocatalyst for PFOA degradation compared to FrCOF-4. This is because defects promote electron-hole recombination and result in poor charge carrier transport properties.

To assess the robustness of FrCOF-4 and its batch-synthesized analogue under irradiation and continuous stirring in acidic conditions, both samples were vigorously stirred for a week following the photocatalytic degradation experiment (UV−C light irradiation for 480 min under continuous stirring) in the degradation byproducts solution. FTIR spectra of the collected and washed FrCOF-4 sample confirmed the intact framework structure, as evidenced by the absence of amino groups and the presence of the imine bond (C□N) with a

stretching band observed at ~1618 cm⁻¹ (Figure S50). PXRD analysis of the collected and washed samples confirmed the

maintained crystalline structure of FrCOF-4 photocatalyst postirradiation and continuous mixing in acidic products (Figure S51). In contrast, FTIR spectra of the collected and washed TAPT-DHTA COF batch-synthesized analogue indicated partial framework degradation, as evidenced by the appearance of amino groups at ~3457 and 3319 cm⁻¹ and a significant reduction in the imine bond intensity at ~1618 cm⁻¹ (Figure S50). Additionally, the PXRD pattern showed a significant loss of crystallinity (Figure S51), which further explains the poor photocatalytic performance of the batch-synthesized analogue compared to FrCOF-4. This chemical stability comparison confirms that FrCOF-4 is an excellent photocatalyst for PFOA degradation, outperforming its batch-synthesized analogue and traditional inorganic photocatalysts in both photocatalytic efficiency and structural robustness.

CONCLUSIONS

We present a flow reactor synthesis strategy based on multiflowing streams for high throughput accelerated synthesis and processing of imine- and hydrazone-linked COFs. This work is distinct from previous COF flow synthesis studies as it combines the continuous synthesis and processing of both imine and hydrazone linkages into a range of macroscopic formats, including monolithic, packed bed formats along with films and prints. In contrast, previous studies utilized either imine or boronate ester linkages in more limited macroscopic formats such as fibers, powders, or thin films. Additionally, this work reports a substantially higher STY of 61,111 kg m³ day⁻¹ and employs a broader range of chemistries (five total; FrCOF-1-5), whereas the previously reported references have much lower STYs and fewer reported chemistries, highlighting the efficiency and versatility of the current microreactor strategy. This methodology can be applied directly to hexagonal imine-linked COFs of all pore sizes without adjustments. We did not study

broader library of COF will require optimizing various reactor parameters, including temperature, flow rate, solvent system, and acid catalyst. Compared with batch synthesis approaches, the flow reactor approach can produce higher yields of COF and, under the right conditions, produce COF of superior crystallinity. However, there are advantages to the batch synthesis approach. The batch synthesis approach is simpler and easier to control. Our flow synthesis approach requires that all reagents be fully soluble to prevent clogging of the flow reactor, which may prevent the synthesis of some COFs. Future research will focus on expanding this platform to a broader range of COF structures with various linkages and topologies. Additionally, we aim to conduct kinetic evaluations to fully understand the implications of flow rate adjustments and refine our synthesis process for enhanced productivities. These efforts will help broaden the library of COFs and facilitate their rapid discovery, making our platform a robust and efficient method for the accelerated screening and synthesis of new COFs.

ASSOCIATED CONTENT

* Supporting Information

The Supporting Information is available free of charge at https://pubs.acs.org/doi/10.1021/acsami.4c09577.

Materials, methods, equations, materials characterization

(PXRD, FTIR, TEM, N₂ sorption analysis, DR-UV-vis,

the synthesis of other topologies of COFs and linking chemistries beyond imine and hydrazone and synthesizing a

55215

PFOA adsorption and photocatalytic degradation experiments and analysis (IC and HPLC) (PDF)

Accelerated movie of COF formation in the flow reactor setup (MP4)

AUTHOR INFORMATION

Corresponding Author

Safiya Khalil — Department of Chemical and Biomolecular Engineering, Rice University, Houston, Texas 77005, United States; orcid.org/0000-0001-6083-7927;

Email: Safiya.khalil@rice.edu

Authors

Abdullah Alazmi – Department of Chemical and Biomolecular Engineering, Rice University, Houston, Texas 77005, United States

Guanhui Gao — Department of Materials Science and NanoEngineering, Rice University, Houston, Texas 77005, United States

Cecilia Martínez-Jiménez — Department of Chemistry, Rice University, Houston, Texas 77005, United States

Ravindra Saxena — Department of Applied Physics, Rice University, Houston, Texas 77005, United States

Yu Chen — Department of Chemical and Biomolecular Engineering, Rice University, Houston, Texas 77005, United States

Shu-Yan Jiang — Department of Chemical and Biomolecular Engineering, Rice University, Houston, Texas 77005, United States; oorcid.org/0000-0003-0159-8385

Jianhua Li — Shared Equipment Authority, Rice University, Houston, Texas 77005, United States

Salma Alhashim — Department of Materials Science and NanoEngineering, Rice University, Houston, Texas 77005, United States

- Thomas P. Senftle Department of Chemical and Biomolecular Engineering, Rice University, Houston, Texas 77005, United States; orcid.org/0000-0002-5889-5009
- Angel A. Martí Department of Materials Science and NanoEngineering, Rice University, Houston, Texas 77005, United States; Department of Chemistry, Rice University, Houston, Texas 77005, United States; Department of Bioengineering, Rice University, Houston, Texas 77005, United States; orcid.org/0000-0003-0837-9855
- Rafael Verduzco Department of Chemical and Biomolecular Engineering, Rice University, Houston, Texas 77005, United States; Department of Materials Science and NanoEngineering, Rice University, Houston, Texas 77005, United States; Nanosystems Engineering Research Center for Nanotechnology-Enabled Water Treatment, Rice University, Houston, Texas 77005, United States; orcid.org/0000-0002-3649-3455

Complete contact information is available at: https://pubs.acs.org/10.1021/acsami.4c09577

Notes

The authors declare no competing financial interest.

ACKNOWLEDGMENTS

S.K. acknowledges support from the Ministry of Education of the United Arab Emirates (UAE). This work was supported by the Welch Foundation for Chemical Research (C-2124). We acknowledge support from the National Science Foundation (NSF), CHE - 2247729. The authors acknowledge Graphic Designer Mario E. Norton (men3@rice.edu), DMC Supervisor, Rice University, for the journal cover art.

REFERENCES

- (1) Côté, A. P.; Benin, A. I.; Ockwig, N. W.; O'Keeffe, M.; Matzger, A. J.; Yaghi, O. M. Chemistry: Porous, Crystalline, Covalent Organic Frameworks. *Science* 2005, *310* (5751), 1166–1170.
- (2) Geng, K.; He, T.; Liu, R.; Dalapati, S.; Tan, K. T.; Li, Z.; Tao, S.; Gong, Y.; Jiang, Q.; Jiang, D. Covalent Organic Frameworks: Design, Synthesis, and Functions. *Chem. Rev.* 2020, *120* (16), 8814–8933.
- (3) Ozdemir, J.; Mosleh, I.; Abolhassani, M.; Greenlee, L. F.; Beitle, R. R.; Beyzavi, M. H. Covalent Organic Frameworks for the Capture, Fixation, or Reduction of CO2. *Front. Energy Res.* 2019, 7, 77.
- (4) Qian, Y.; Ma, D. Covalent Organic Frameworks: New Materials Platform for Photocatalytic Degradation of Aqueous Pollutants. *Materials* 2021, *14* (19), 5600.
- (5) Guo, J.; Jiang, D. Covalent Organic Frameworks for Heterogeneous Catalysis: Principle, Current Status, and Challenges. *ACS Cent. Sci.* 2020, 6 (6), 869–879.
- (6) Li, J.; Zhou, X.; Wang, J.; Li, X. Two-Dimensional Covalent Organic Frameworks (COFs) for Membrane Separation: A Mini Review. *Ind. Eng. Chem. Res.* 2019, *58*, 15394.
- (7) Chen, S.; Yuan, B.; Liu, G.; Zhang, D. Electrochemical Sensors Based on Covalent Organic Frameworks: A Critical Review. *Front. Chem.* 2020, *8*, 601044.
- (8) Liu, Y. Yi Liu Answers Questions about 15 Years of Research on Covalent Organic Frameworks. *Nat. Commun.* 2020, *11* (1), 5333.
- (9) Zou, X. Xiaodong Zou Answers Questions about 15 Years of Research on Covalent Organic Frameworks. *Nat. Commun.* 2020, *11* (1), 5330.
- (10) Shustova, N. B. Natalia Shustova Answers Questions about 15 Years of Research on Covalent Organic Frameworks. *Nat. Commun.* 2020, *11* (1), 5329.
- (11) Zhao, W.; Xia, L.; Liu, X. Covalent Organic Frameworks (COFs): Perspectives of Industrialization. *CrystEngcomm* 2018, 20 (12), 1613–1634.

- (12) Li, X.; Yang, C.; Sun, B.; Cai, S.; Chen, Z.; Lv, Y.; Zhang, J.; Liu, Y. Expeditious Synthesis of Covalent Organic Frameworks: A Review. *J. Mater. Chem. A* 2020, *8*, 16045.
- (13) Martinez-Bulit, P.; Sorrenti, A.; Rodriguez, D.; Mattera, M.; Belce, Y.; Xia, Y.; Ma, S.; Huang, M.-H.; Pané, S.; Puigmartí-Luis, J. In Flow-Based Technologies: A New Paradigm for the Synthesis and Processing of Covalent-Organic Frameworks. *Chem. Eng. J.* 2022, 435, 135117–135117.
- (14) Rodríguez-San-Miguel, D.; Zamora, F. Processing of Covalent Organic Frameworks: An Ingredient for a Material to Succeed. *Chem. Soc. Rev.* 2019, 48, 4375.
- (15) Hu, J.; Huang, Z.; Liu, Y. Beyond Solvothermal: Alternative Synthetic Methods for Covalent Organic Frameworks. *Angew. Chem., Int. Ed.* 2023, *62*, No. e202306999.
- (16) Liu, Z.; Zhu, J.; Peng, C.; Wakihara, T.; Okubo, T. Continuous Flow Synthesis of Ordered Porous Materials: From Zeolites to Metal—Organic Frameworks and Mesoporous Silica. *React. Chem. Eng.* 2019, *4* (10), 1699–1720.
- (17) Tsubogo, T.; Oyamada, H.; Kobayashi, S. Multistep Continuous-Flow Synthesis of (R)- and (S)-Rolipram Using Heterogeneous Catalysts. *Nature* 2015, *520* (7547), 329–332.
- (18) PNAS. Continuous flow synthesis of ZSM-5 zeolite on the order of seconds, PNAS. https://www.pnas.org/doi/full/10.1073/pnas. 1615872113. (Accessed 23 May 2024).
- (19) Rubio-Martinez, M.; Batten, M. P.; Polyzos, A.; Carey, K. C.; Mardel, J. I.; Lim, K. S.; Hill, M. R. Versatile, High Quality and Scalable Continuous Flow Production of Metal-Organic Frameworks. *Sci. Rep.* 2014, *4*, 5443.
- (20) Bagi, S.; Yuan, S.; Rojas-Buzo, S.; Shao-Horn, Y.; Román-Leshkov, Y. A Continuous Flow Chemistry Approach for the Ultrafast and Low-Cost Synthesis of MOF-808. *Green Chem.* 2021, 23 (24), 9982–9991.
- (21) Bayliss, P. A.; Ibarra, I. A.; Pérez, E.; Yang, S.; Tang, C. C.; Poliakoff, M.; Schröder, M. Synthesis of Metal—Organic Frameworks by Continuous Flow. *Green Chem.* 2014, *16* (8), 3796—3802.
- (22) Haase, F.; Lotsch, B. V. Solving the COF Trilemma: Towards Crystalline, Stable and Functional Covalent Organic Frameworks. *Chem. Soc. Rev.* 2020, *49*, 8469–8500.
- (23) Rodríguez-San-Miguel, D.; Abrishamkar, A.; Navarro, J. A. R.; Rodriguez-Trujillo, R.; Amabilino, D. B.; Mas-Ballesté, R.; Zamora, F.; Puigmartí-Luis, J. Crystalline Fibres of a Covalent Organic Framework through Bottom-up Microfluidic Synthesis. *Chem. Commun.* 2016, *52* (59), 9212–9215.
- (24) Peng, Y.; Wong, W. K.; Hu, Z.; Cheng, Y.; Yuan, D.; Khan, S. A.; Zhao, D. Room Temperature Batch and Continuous Flow Synthesis of Water-Stable Covalent Organic Frameworks. *Chem. Mater.* 2016, *28* (14), 5095–5101.
- (25) Bisbey, R. P.; Deblase, C. R.; Smith, B. J.; Dichtel, W. R. Two-Dimensional Covalent Organic Framework Thin Films Grown in Flow. *J. Am. Chem. Soc.* 2016, *138*, 11433–11436.
- (26) Khalil, S.; Meyer, M. D.; Alazmi, A.; Samani, M. H. K.; Huang, P.-C.; Barnes, M.; Marciel, A. B.; Verduzco, R. Enabling Solution Processable COFs through Suppression of Precipitation during Solvothermal Synthesis. *ACS Nano* 2022, *16* (12), 20964–20974.
- (27) Summary of Key Physical Data for Solvents. https://www.fishersci.co.uk/gb/en/scientific-products/technical-tools/summary-key-physical-data-solvents.html. (Accessed 12 August 2024).
- (28) Feriante, C.; Evans, A. M.; Jhulki, S.; Castano, I.; Strauss, M. J.; Barlow, S.; Dichtel, W. R.; Marder, S. R. New Mechanistic Insights into the Formation of Imine-Linked Two-Dimensional Covalent Organic Frameworks. *J. Am. Chem. Soc.* 2020, *142*, 18637–18644.
- (29) Li, R. L.; Flanders, N. C.; Evans, A. M.; Ji, W.; Castano, I.; Chen, L. X.; Gianneschi, N. C.; Dichtel, W. R. Controlled Growth of Imine-Linked Two-Dimensional Covalent Organic Framework Nanoparticles. *Chem. Sci.* 2019, *10* (13), 3796–3801.
- (30) Smith, B. J.; Parent, L. R.; Overholts, A. C.; Beaucage, P. A.; Bisbey, R. P.; Chavez, A. D.; Hwang, N.; Park, C.; Evans, A. M.; Gianneschi, N. C.; Dichtel, W. R. Colloidal Covalent Organic Frameworks. *ACS Cent. Sci.* 2017, *3* (1), 58–65.

- (31) Segura, J. L.; Royuela, S.; Ramos, M. M. Post-Synthetic Modification of Covalent Organic Frameworks. *Chem. Soc. Rev.* 2019, 48, 3903–3945
- (32) Zhu, D.; Zhang, J. J.; Wu, X.; Yan, Q.; Liu, F.; Zhu, Y.; Gao, X.; Rahman, M. M.; Yakobson, B. I.; Ajayan, P. M.; Verduzco, R. Understanding Fragility and Engineering Activation Stability in Two-Dimensional Covalent Organic Frameworks. *Chem. Sci.* 2022, *13* (33), 9655–9667.
- (33) Qian, Y.; Han, Y.; Zhang, X.; Yang, G.; Zhang, G.; Jiang, H.-L. Computation-Based Regulation of Excitonic Effects in Donor-Acceptor Covalent Organic Frameworks for Enhanced Photocatalysis. *Nat. Commun.* 2023, *14* (1), 3083.
- (34) Hu, S.-Y.; Sun, Y.-N.; Feng, Z.-W.; Wang, F.-O.; Lv, Y. Design and Construction Strategies to Improve Covalent Organic Frameworks Photocatalyst's Performance for Degradation of Organic Pollutants. *Chemosphere* 2022, 286, 131646.
- (35) Chen, Z.; Li, Y.; Cai, Y.; Wang, S.; Hu, B.; Li, B.; Ding, X.; Zhuang, L.; Wang, X. Application of Covalent Organic Frameworks and Metal—Organic Frameworks Nanomaterials in Organic/Inorganic Pollutants Removal from Solutions through Sorption-Catalysis Strategies. *Carbon Res.* 2023, *2* (1), 8.
- (36) Žhu, Y.; Zhu, D.; Chen, Y.; Yan, Q.; Liu, C. Y.; Ling, K.; Liu, Y.; Lee, D.; Wu, X.; Senftle, T. P.; Verduzco, R. Porphyrin-Based Donor–Acceptor COFs as Efficient and Reusable Photocatalysts for PET-RAFT Polymerization under Broad Spectrum Excitation. *Chem. Sci.* 2021, *12* (48), 16092–16099.
- (37) Wang, X.; Chen, L.; Chong, S. Y.; Little, M. A.; Wu, Y.; Zhu, W.-H.; Clowes, R.; Yan, Y.; Zwijnenburg, M. A.; Sprick, R. S.; Cooper, A. I. Sulfone-Containing Covalent Organic Frameworks for Photocatalytic Hydrogen Evolution from Water. *Nat. Chem.* 2018, *10* (12), 1180–1189.
- (38) Jhulki, S.; Evans, A. M.; Hao, X.-L.; Cooper, M. W.; Feriante, C. H.; Leisen, J.; Li, H.; Lam, D.; Hersam, M. C.; Barlow, S.; Brédas, J.-L.; Dichtel, W. R.; Marder, S. R. Humidity Sensing through Reversible Isomerization of a Covalent Organic Framework. *J. Am. Chem. Soc.* 2020, *142* (2), 783–791.